Supplementary Material of "Machine-learning-enhanced automatic spectral characterization of x-ray pulses from a free-electron laser"

Danilo Enoque Ferreira de Lima*,[a] Arman Davtyan, Joakim Laksman, Natalia Gerasimova, Theophilos Maltezopoulos, Jia Liu, Philipp Schmidt, Thomas Michelat, Tommaso Mazza, Michael Meyer, Jan Grünert, and Luca Gelisio
European XFEL, Schenefeld, 22869, Germany

SI. SASE3 X-RAY SPECTROMETERS

The grating-based monochromator can operate in spectrometer mode (GS)[1] by introducing a YAG:Ce crystal in its focal plane, which converts the x-ray photons into optical luminescence. The resulting image is registered by a standard CCD camera. This diagnostic monitor is called the exit slit imager, which provides an optical system, including a fast electronic shutter, that can be applied to select a single pulse from a pulse train[2], much like an image intensifier. The resulting images are used to measure the X-ray spectrum in the focal plane of the monochromator. We refer to Refs.[1,3] for further details on the GS.

The operation principle of the photo-electron spectrometer (PES) is that atoms in a low density matter target – typically a very dilute gas – are ionized whereupon photo-electrons are emitted with a kinetic energy that is related to the photon energy[4]. Flight-tubes composed of four electrostatic sections with an applied retardation potential act as dispersive elements where the time is measured from the instant of ionization until electrons reach a micro-channel plate (MCP) based detector. Instrumental resolution is limited by the fact that retardation takes place stepwise in each segment, thus higher retardation voltage cannot fully compensate for higher initial kinetic energy. This implies that lower photo-electron kinetic energy has higher temporal dispersion and consequently higher spectral resolving power[5]. Criteria for selecting target gas for a particular photon energy are, in addition to low photo-electron kinetic energy, also high photo-ionization cross-section[6] (σ) for improved signal to noise ratio and narrow Lorentzian lifetime broadening[7] (Γ). Flight-tubes are assembled in a plane oriented perpendicular with respect to the X-ray beam. The angular distribution of the photo-electrons depends on the anisotropy parameter β for the electronic transition of the target gas[8]. Available target gases are N_2, Ne, Kr, and Xe.

Data acquisition is performed with digitizer boards (SP Devices ADQ 412-4G) in a μTCA crate. Each board can be operated acquiring data from all channels with a sampling rate of $2\,\mathrm{GSs}^{-1}$ (500 ps binning), or optionally two channels can be bridged (interleaved mode) in order to increase the rate to $4\,\mathrm{GSs}^{-1}$ (250 ps binning). We refer to Ref.[5] for further details on the PES.

SII. EXPERIMENTAL DETAILS

This section includes information on XFEL characteristics and PES settings for the experimental data used in the manuscript. In particular, Tab. S1 lists the data-taking configurations for each dataset used. All the data were collected in the context of commissioning proposals at European XFEL.

Dataset D_H uses the N_2 1s transition at photon energies around 900 eV with $\sigma \approx 0.09\,\mathrm{Mb}$, $\Gamma = 0.13\,\mathrm{eV}$[7], and $\beta = 2.0$. The binding energy is 410 eV. Dataset D_I includes data taken using the Xe $3d_{3/2}$ (with a binding energy of 689 eV, $\Gamma = 0.468\,\mathrm{eV}$) and $3d_{5/2}$ (with a binding energy of 676.4 eV, $\Gamma = 0.482\,\mathrm{eV}$) at photon energies around 1400 eV with $\sigma \approx 0.6\,\mathrm{Mb}$ and $\beta = 1.13$. The spectral bandwidth in Xe is less than 10 eV, and thus the spin-orbit splitting of 12.6 eV is sufficient to avoid overlap in the time-of-flight spectra. All remaining datasets use the Ne 1s transition, which has a binding energy of approximately 870 eV.

SIII. EXAMPLE RESULTS

The spectra of the samples highlighted in Fig. 4 of the main text are shown in Fig. S1.

[a] Electronic mail: danilo.enoque.ferreira.de.lima@xfel.eu

Dataset	Undulator		Average of pulse		PES				
	Cells	Taper	Pulse energy [mJ]	Photon energy [eV]	Gas	Pressure [$\times 10^{-6}$ mbar]	Retard. pot. [V]	Samp. rate [GSs^{-1}]	Channels
D_A[9]	10	Linear	1.3	1001	Ne	1.3	-116	2	12
D_B[9]	8	Linear	0.6	917	Ne	0.9	-35	2	12
D_C[9]	9	Linear	2.0	892	Ne	0.2	0	2	12
D_D[9]	13	Quadratic	4.1	917	Ne	0.3	-36	2	12
D_E[9]	7	Linear	0.05	917	Ne	9.5	-35	2	12
D_F[9]	9	Linear	2.0	892	Ne	0.2	0	4	6
D_G[9]	11	Quadratic	1.9	917	Ne	0.4	-35	2	12
D_H[9]	9	Linear	1.4	895	N_2	1.7	-480	2	12
D_I[9]	9	Linear	0.2	1391	Xe	5.5	-689	2	12
D_J[9]	9	Linear	1.7	916	Ne	5	-36	2	12

TABLE S1. Operating conditions for the datasets used in this study. For each row two samples were derived, one that was used for training of the virtual spectrometer (VS), and another one which was used (under the same operating conditions) for validating the results during inference. The column "Dataset" shows the dataset identifier used in the paper. The columns "Cells" and "Taper" show the number of undulator cells used, and the taper configuration, respectively. These parameters strongly influence the x-ray properties. The average x-ray pulse energy ("Energy") and photon energy ("Ph, energy") are also reported. The remaining columns refer to the PES settings and include the gas used ("Gas") and its pressure ("Pressure"), the electric potential used to control the electric field in the PES ("Retard. pot."), the PES data acquisition rate in units of a billion samples per second ("Samp. rate"); and the number of PES channels acquired ("Channels"). When operating in interleaved mode, the sampling rate is twice higher as in normal operation, and only half of the channels are available.

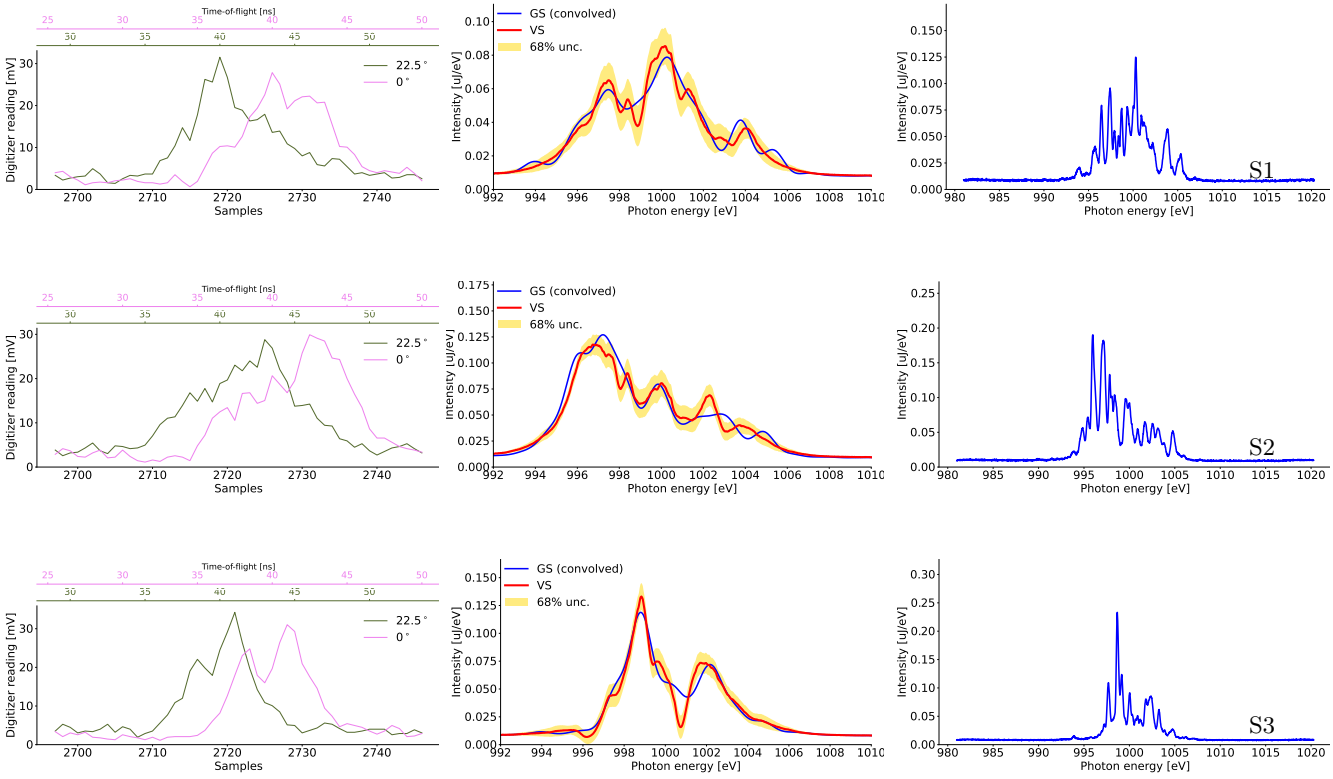

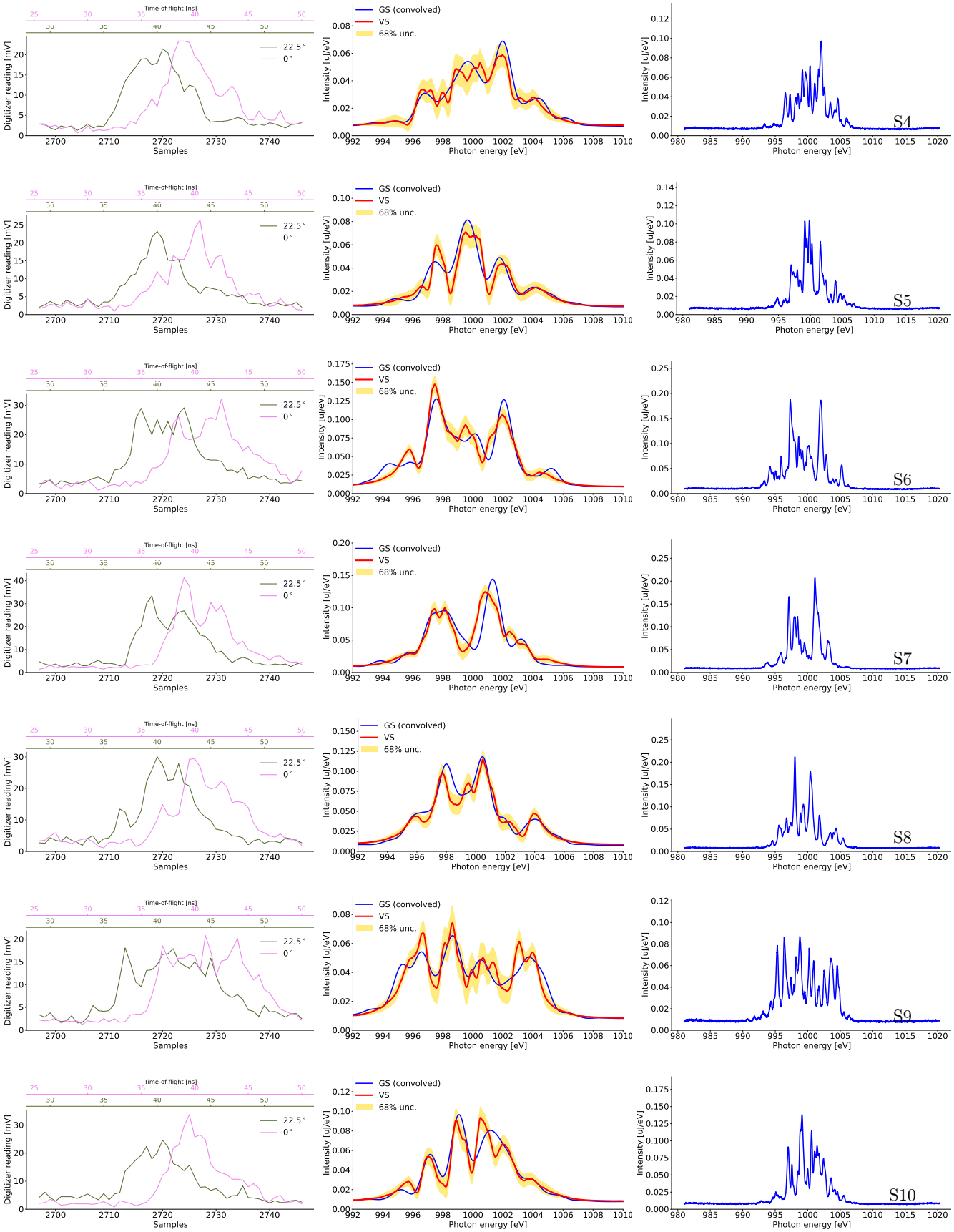
Time-of-flight [ns]
Digitizer reading [mV]
Samples
22.5 °
0 °
GS (convolved)
VS
68% unc.
Intensity [uJ/eV]
Photon energy [eV]
S4
S5
S6
S7
S8
S9
S10

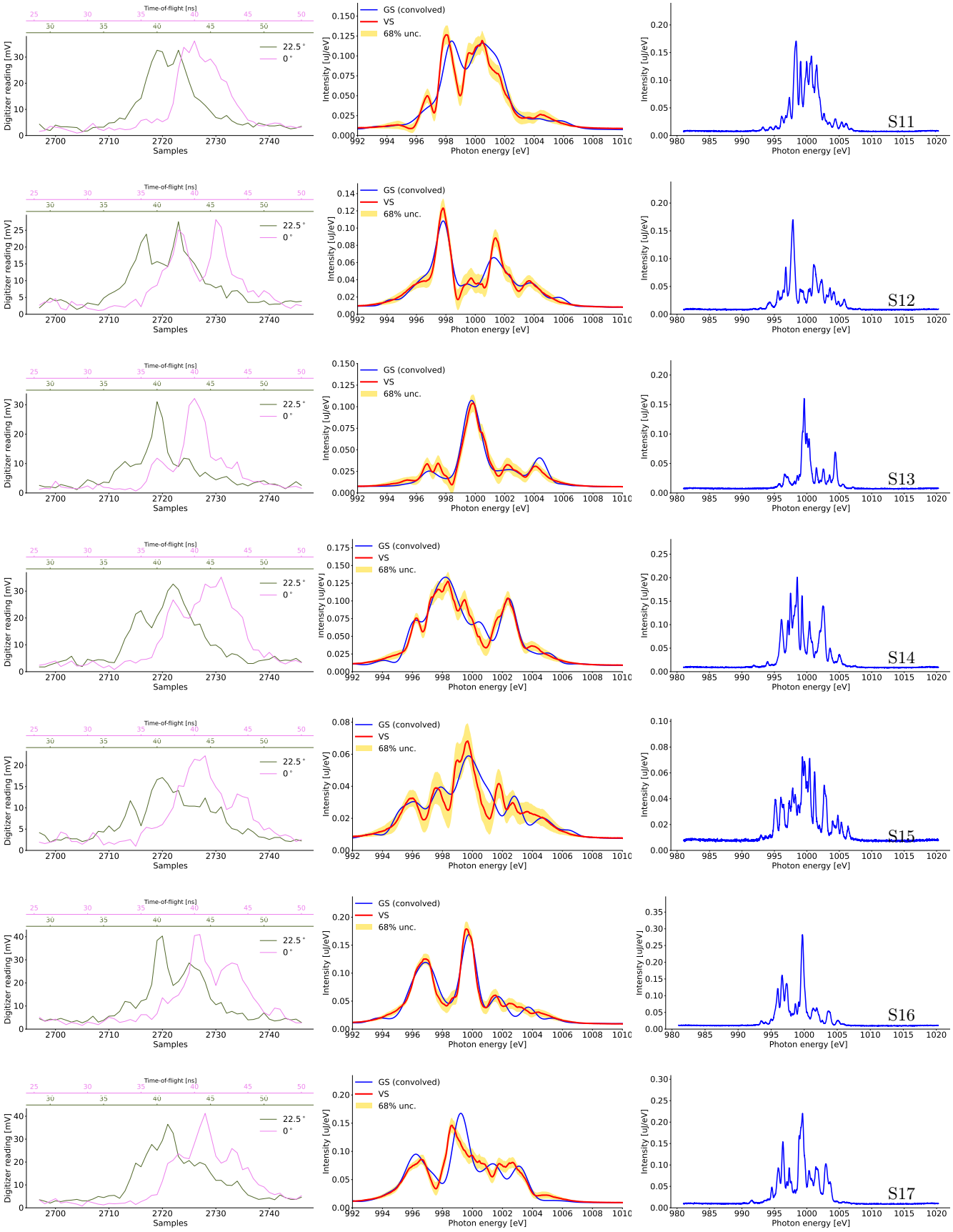
Time-of-flight [ns]
Digitizer reading [mV]
Samples
22.5 °
0 °
GS (convolved)
VS
68% unc.
Intensity [uJ/eV]
Photon energy [eV]
S11
S12
S13
S14
S15
S16
S17

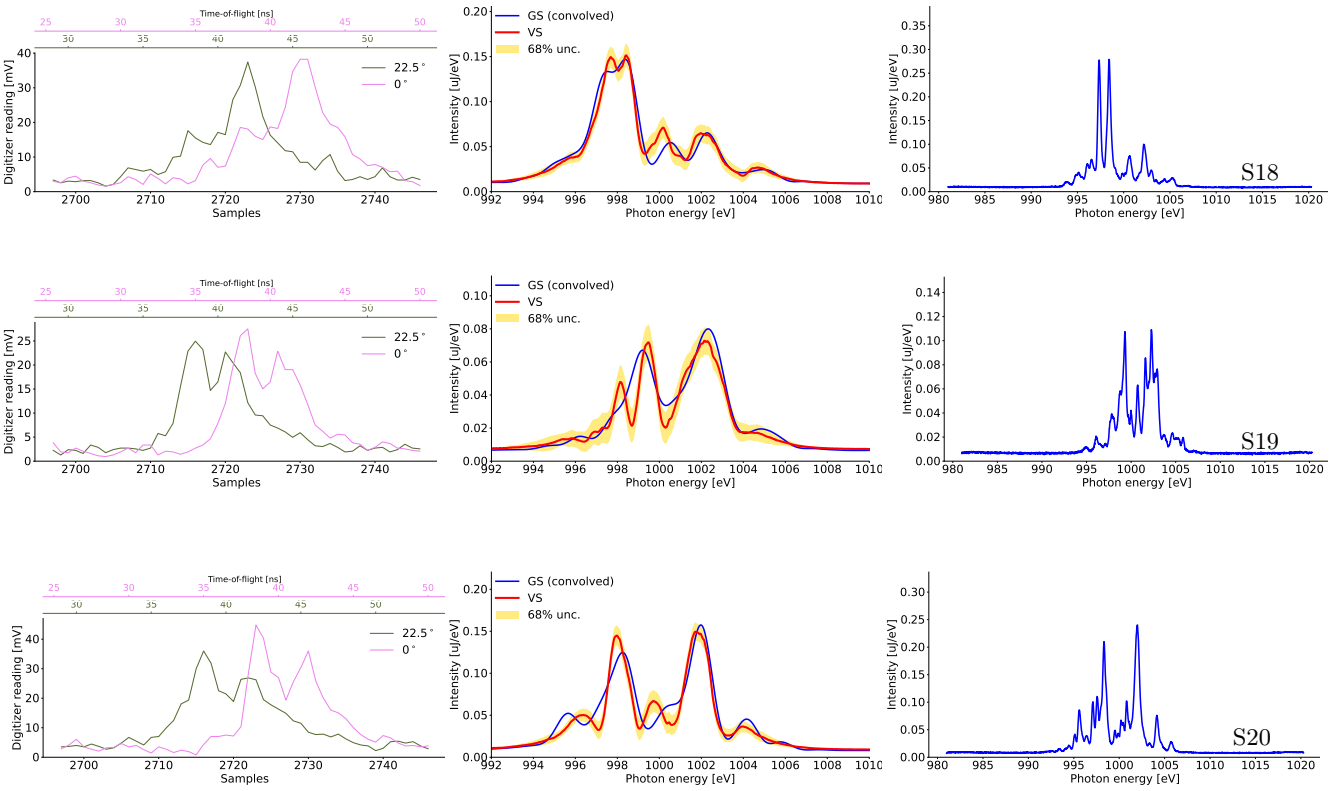

(a) Measured PES data. (b) VS and smoothened GS data. (c) GS data.

FIG. S1. Test dataset D_A. The sample identification number (corresponding to Fig. 4) is given in the right bottom part of each row. (a) PES time-of-flight measurements. Two of the measured channels (PES sub-detectors) is shown. (b) Virtual spectrometer output for the same sample. The blue solid line shows the GS measurement smoothened by the VS response function. The red line shows the mean prediction of the VS considering only the PES data for this train, after training. The yellow band shows the 68% confidence level uncertainty band around the prediction. (c) Original GS data.

SIV. CHOICE OF HYPER-PARAMETERS

The most important free hyper-parameters of the method include those of the automatic relevance determination (ARD)[10] fit, and the number of principal components[11]. The ARD fit uses expectation maximization to solve the Bayes' theorem and determines the weights and uncertainties a posteriori. It relies on the choice of shape and scale parameters for the Gamma distribution hyper-prior. The choice of hyper-prior parameters has been done following the criterium for an uninformative prior[12], according to which the hyper-prior should provide the least amount of information possible, to avoid biasing the fit. According to such criteria, the scale and rate parameters of the Gamma hyper-prior have been set to be as close to zero as possible, to the value of 10^{-6} (a value of exactly zero would lead to an undefined distribution). In addition, the threshold used to prune weights with large uncertainties has been set to a precision of 10^4.

The number of principal components is chosen after analysing the cumulative variance contained in the components, as shown, for example, in Fig. S2 for dataset D_A. The dashed line shows the point of the cumulative variance curve corresponding to 90% of the variance. Notice that the curve reaches an asymptotic behaviour and adding more features does not increase significantly the variance content. As we would like to remove low-variance content, the threshold at 90% has been chosen to keep most of the variance.

The GS has 1800 measurement points, which, for dataset D_A, have been reduced to only 24 components after the projection into the leading principal components. The region-of-interest selection in the PES provides 600 features per channel, which are augmented with the pulse intensity. While the PES is capable of performing measurements in 16 channels in total, only 12 channels have been used in this test (see Tab. S1). 600 PES principal components have been kept. The threshold on the PCA variance is chosen such that sufficient data for a stable and fast fit is provided.

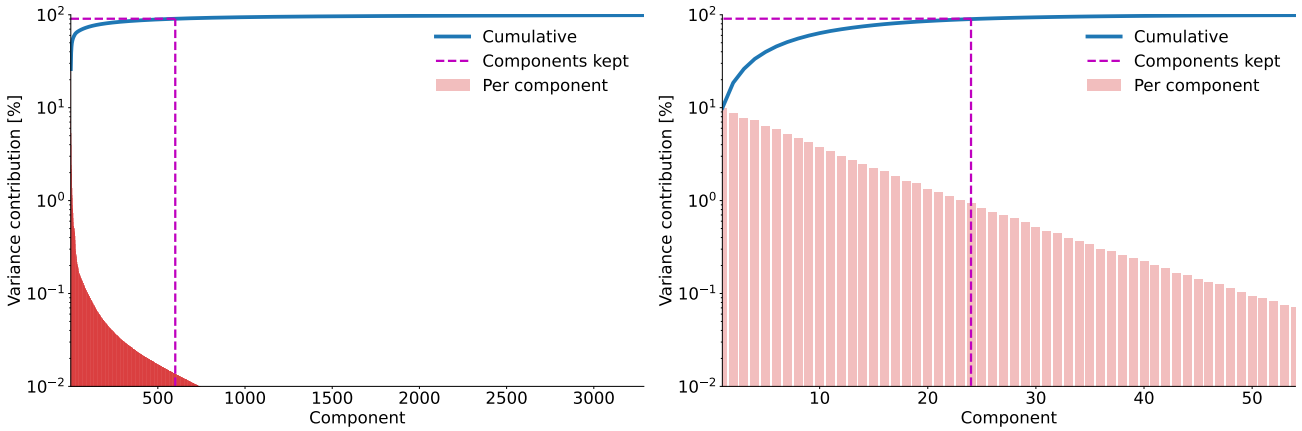

(a) Photo-electron spectrometer.

(b) Grating-based spectrometer.

FIG. S2. Variance contained in each principal component (red) and the cumulative variance contained up until the given component (blue) for dataset D_A. Components are ordered by their corresponding eigenvalues. (a) effect of PCA on PES data. (b) effect of PCA on GS data. The dashed lines correspond to a 90% cumulative variance.

SV. RESOLUTION ESTIMATION METHOD

This section summarizes the procedure used for the resolution estimation from the spectral data collected at European XFEL, which often contains many spectral modes. In this analysis we have the advantage of having a reference spectrum from the GS, which can be used to estimate the effect of the VS with very mild assumptions.

We have several estimates of the photon energy spectrum from GS measurements, $\mathbf{y}$, and from VS, $\hat{\mathbf{y}}$. It is assumed that the VS result is a degraded version of the GS measurement, as a result of convolving the GS spectra with a response function. Mathematically, we model such effect as

$$\begin{aligned} \hat{\mathbf{y}} &= (\mathbf{h} \circledast \mathbf{y}) + \mathbf{n}, \\ \hat{\mathbf{Y}} &= \mathbf{H}\,\mathbf{Y} + \mathbf{N}, \end{aligned} \tag{1}$$

where $\circledast$ is the convolution operator, and $\mathbf{h}$ is the response function, which encodes the effect of such degradation. The term $\mathbf{n}$ encodes all effects that cannot be modelled in such a manner. The same equation is rewritten in the second line in terms of the Fourier transforms of $\hat{\mathbf{y}}$ $\mathbf{y}$, $\mathbf{h}$, and $\mathbf{n}$, which are written as $\hat{\mathbf{Y}}$, $\mathbf{Y}$, $\mathbf{H}$, and $\mathbf{N}$, respectively.

One could calculate $\mathbf{H}$ as $\frac{\hat{\mathbf{Y}}-\mathbf{N}}{\mathbf{Y}}$, however we do not have an estimate of the noise level per spectrum. Additionally, if one ignores the noise term, the estimate of $\mathbf{H}$ would include a term inversely proportional to the signal-to-noise ratio. We avoid this by calculating the cross power spectral density, $S_{\mathbf{y}\hat{\mathbf{y}}}$, defined as $\mathbb{E}\left[\mathbf{Y}^*\,\hat{\mathbf{Y}}\right]$. Namely,

$$\begin{aligned} S_{\mathbf{y}\hat{\mathbf{y}}} &\triangleq \mathbb{E}\left[\mathbf{Y}^*\,\hat{\mathbf{Y}}\right] \\ &= \mathbb{E}\left[\mathbf{Y}^*\mathbf{H}\mathbf{Y} + \mathbf{Y}^*\mathbf{N}\right] \\ &= \mathbf{H}\,\mathbb{E}\left[\mathbf{Y}^*\mathbf{Y}\right] + \mathbb{E}\left[\mathbf{Y}^*\mathbf{N}\right] \\ &= \mathbf{H}\,\mathbb{E}\left[\mathbf{Y}^*\mathbf{Y}\right] \\ &= \mathbf{H}\,S_{\mathbf{yy}}. \end{aligned}$$

In this calculation, the assumption has been made that the noise is uncorrelated with $\hat{\mathbf{y}}$. As a result, one may estimate $\mathbf{h}$ as:

$$\begin{aligned} \mathbf{h} &= \mathcal{F}^{-1}\left\{\frac{S_{\mathbf{y}\hat{\mathbf{y}}}}{S_{\mathbf{yy}}}\right\}, \\ \mathbf{h} &= \mathcal{F}^{-1}\left\{\frac{\mathbb{E}\left[\mathbf{Y}^*\,\hat{\mathbf{Y}}\right]}{\mathbb{E}\left[\mathbf{Y}^*\,\mathbf{Y}\right]}\right\}, \end{aligned} \tag{2}$$

where $\mathcal{F}^{-1}$ represents the inverse Fourier transform. To avoid noise and numerical fluctuations, Welch's method[13] is used to estimate the cross-spectral density and spectral density estimates, with a Hamming window size of 400.

This procedure can be done after multiplying the spectra $\mathbf{y}$ and $\hat{\mathbf{y}}$ by a Super-Gaussian of degree 2 to emphasize a given energy range and thereby, produce an estimate of $\mathbf{h}$ for different energy regimes. The full-width-at-half-maximum of $\mathbf{h}$ is used as an estimate of the resolution.

It is important to note that the function $\mathbf{h}$ may be arbitrarily small. That is, if there is a very low signal-to-noise ratio, the first term of Eq. 2 may contain a very narrow function $\mathbf{h}$, but with a very small normalization factor, in which case the noise term, $\mathbf{n}$, dominates. We can use a similar approach as above to estimate the mean signal-to-noise ratio in $\hat{\mathbf{y}}$, which provides an idea of how many effects cannot be modelled by a resolution model. Namely, we estimate the signal component, σ_s, and the noise component, σ_n, using:

$$\sigma_s = \sqrt{\frac{1}{N_{\text{bins}}} \sum_{\text{bins}} \mathbb{E}\left[|\mathbf{HY}|^2\right]},$$
$$\sigma_n = \sqrt{\frac{1}{N_{\text{bins}}} \sum_{\text{bins}} S_{\hat{\mathbf{y}}\hat{\mathbf{y}}} - \sigma_s^2},$$

where N_{bins} is the number of bins, and the equation for the noise level follows from Eq. 2. The mean signal-to-noise level can be estimated as $\frac{\sigma_s}{\sigma_n}$.

More information on the methods and statistical definitions can be found in more details in classical signal processing textbooks[14].

SVI. VALIDATION OF THE RESOLUTION ESTIMATE

Although the shape of the resolution function is not perfectly Gaussian, we have cross-checked the obtained results, by smearing the original grating spectrometer spectra with a Gaussian of different widths, and comparing the smeared GS with the VS. The comparison was done by estimating the average root-mean-squared error between the unit-normalized spectra. If $\mathbf{h}$ were indeed Gaussian, the GS and the VS results should have the lowest root-mean-squared error when the grating spectrometer measurement is smeared by a Gaussian with the correct resolution width. The result is shown in Fig. S3 and Fig. S4. The red dashed line shows the results using the method described in Sec. SV. Although the function h is not Gaussian, the minimum of the curve is quite close to the resolution obtained using the method in Sec. SV.

SVII. IMPACT OF NOISE ON THE RESOLUTION ESTIMATE

While Sec. SV discusses how to estimate the resolution of the VS, there are effects that are not modelled by the resolution. This could be the non-detection of a peak, due to the large noise content in the PES, as well as any other effects not captured in the resolution model. For this reason, Sec. SV also includes details on the calculation of a signal-to-noise ratio. Figure S5 shows the signal-to-noise ratio of the VS result versus the average resolution for each dataset.

SVIII. TRADE-OFF BETWEEN NOISE AND RESOLUTION

A low signal-to-noise ratio indicates that there are effects not captured by the resolution model. That is, artefacts may appear in the PES measurements and propagated to the VS output. One can reduce the impact of such artefacts, by convolving the grating spectrometer data by a Gaussian, so that effects across a wider range of photon energy are emphasized. While this undoubtedly reduces the final resolution of the VS, it increases its signal-to-noise ratio. Fig. S6 shows the effect of the full-width-at-half-maximum of a Gaussian in both the resolution and signal-to-noise ratio of different datasets. Scientists may optimize for a signal-to-noise ratio, sacrificing resolution by tuning the VS accordingly.

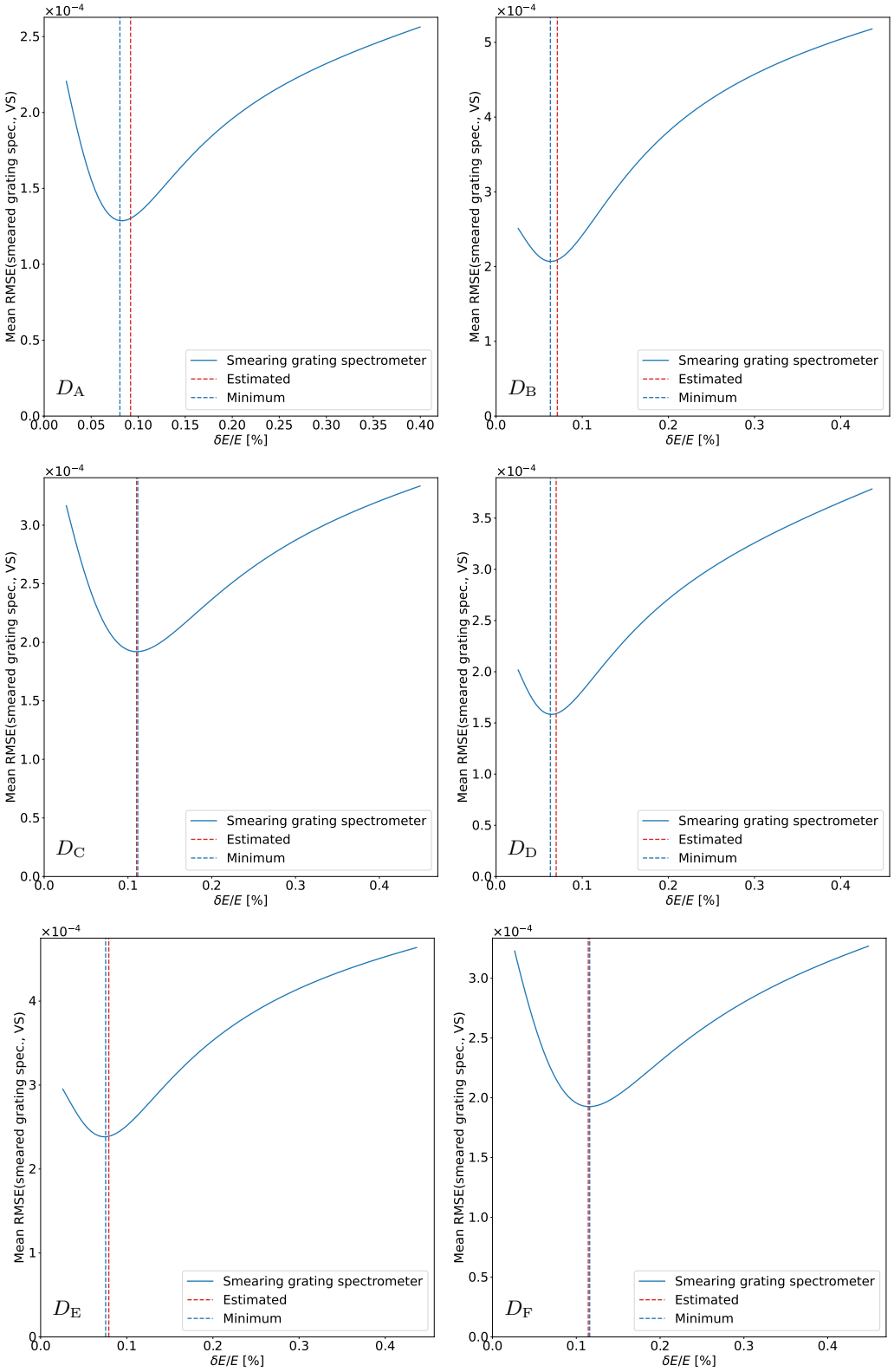

FIG. S3. Average root-mean-squared difference between smeared GS output and VS estimate versus the full-width-at-half-maximum (FWHM) of the smearing Gaussian used in dataset D_A – D_F. The red dashed line shows the FWHM obtained using the method described in Sec. SV for comparison.

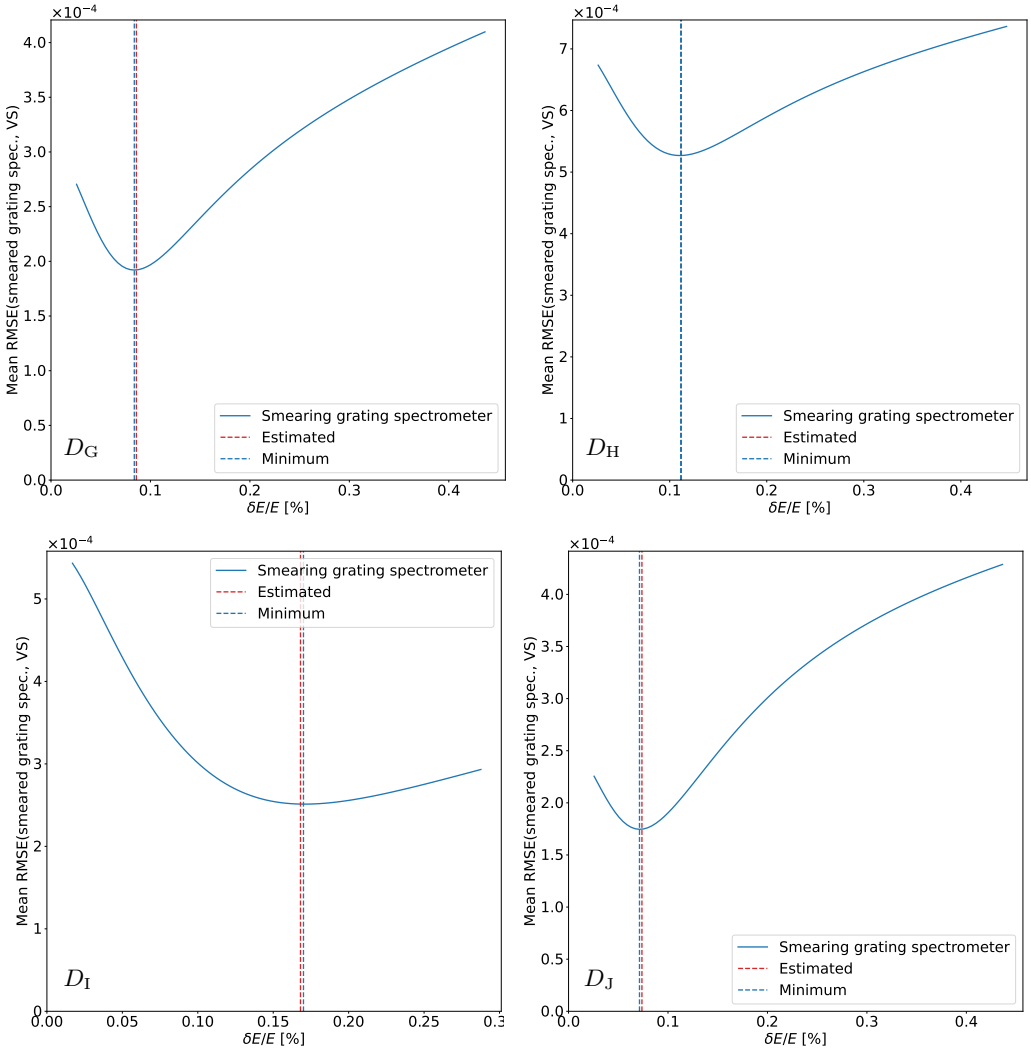

FIG. S4. Average root-mean-squared difference between smeared GS output and VS estimate versus the full-width-at-half-maximum (FWHM) of the smearing Gaussian used in dataset D_G – D_J. The red dashed line shows the FWHM obtained using the method described in Sec. SV for comparison.

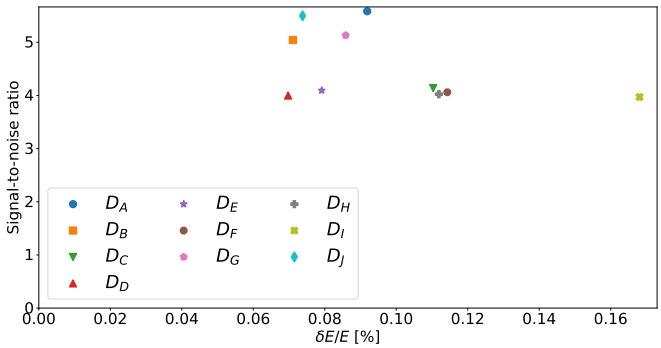

FIG. S5. Signal-to-noise ratio of the VS output versus resolution.

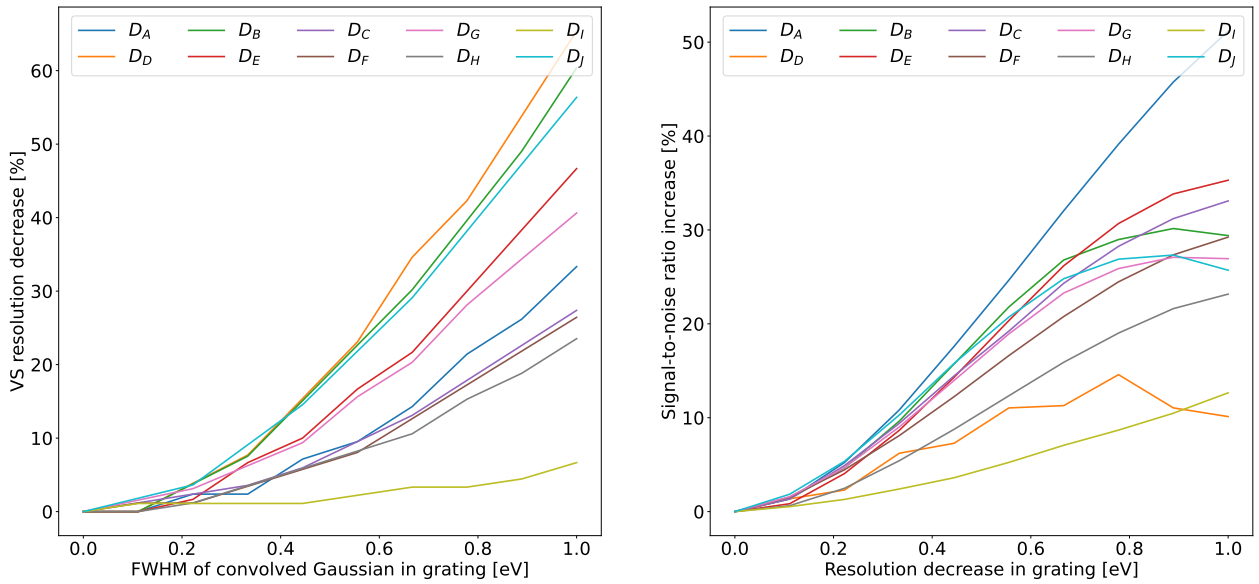

(a) Impact on the Virtual Spectrometer resolution.

(b) Impact on signal-to-noise ratio.

FIG. S6. Effect of pre-smoothing the GS on the VS resolution (a), and the signal-to-noise ratio (b).

SIX. STATISTICAL SIMULATION DETAILS

To better understand the increase of resolution of the VS with respect to the GS, we have generated artificial datasets under controlled conditions. As such, we define the PES calibration function.

We have simulated spikes in random positions with higher probability in the middle of the energy range, according to a Normal distribution with standard deviation given by half of the energy range. For each pulse, the number of spikes is taken from a Poisson distribution with mean 10, and the peak amplitude is sampled from a Gamma distribution with scale parameter 0.15 and shape parameter 2. The spectra are normalized by the simulated pulse energy, taken to be samples of a Normal distribution with mean 1.3 mJ and standard deviation of 200 µJ. These spectra are smoothed to produce grating spectrometer observations, by convolving them with a Gaussian corresponding to a resolution of 0.6 eV to simulate the effect of both the FEL bandwidth and the grating spectrometer resolution. Normally-distributed white noise is added with a standard deviation of 2.

The PES observation is obtained by smearing the grating spectrometer result with a Gaussian of 1.6 eV FWHM. The resulting spectrum is converted to a time-of-flight observation with true calibration constants set to the same as the ones obtained for dataset D_A. The final PES samples are scaled by the squared cosine of the PES detector angle to simulate the polarization effect, scaled to simulate the cross-section and acceptance effects. Additionally, as the PES estimates photo-electron counts, the simulation of the statistical uncertainty is done by taking a sample from a Poisson distribution corresponding to the number of detected photo-electrons. Extra Gaussian noise is added with standard deviation of 1 count to simulate the electronic noise in the PES. Examples of simulated PES and GS measurements, and the corresponding VS result are shown in Figure S7.

SX. IMPLEMENTATION WITHIN THE KARABO CONTROL SYSTEM

Fig. S8 shows the easy-to-use and automated graphical interface for both training the model and performing inference while the experiment progresses, as data arrives. This is implemented within European XFEL's control system Karabo[15]. Notice that Fig. S8b displays two plots and a lamp icon: variations of the input data quality are estimated and an alarm is triggered if needed (the green lamp becomes red). Fig. S8a shows the resolution and signal-to-noise ratio estimates.

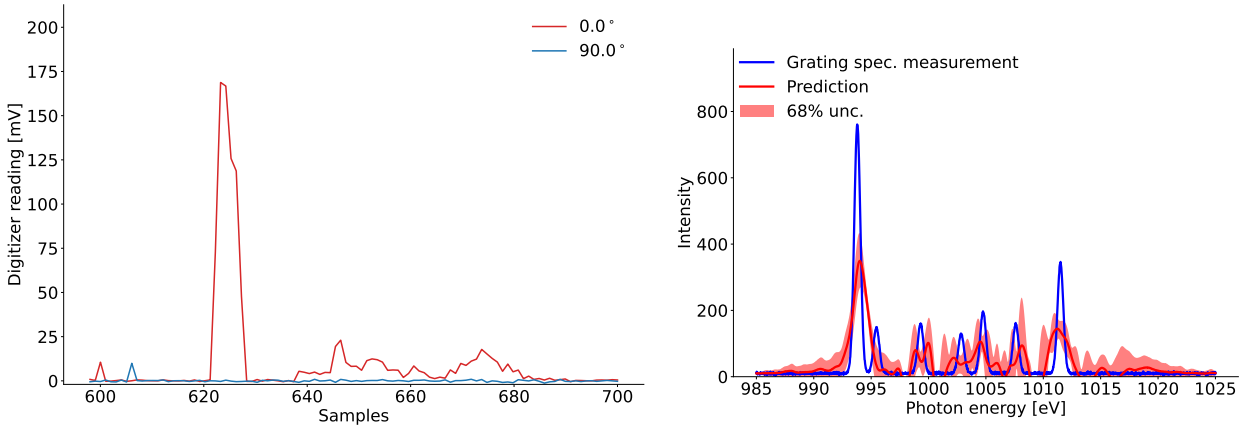

(a) Example simulation of the PES.

(b) Example application of the VS on simulated data in (a).

FIG. S7. (a) Example of simulated calibrated PES data, and (b) application of the VS to data in (a).

SXI. AVERAGE SPECTRA

Fig. S9 shows the mean spectra and their root-mean-squared error obtained for each dataset. The mean spectra corresponds to the sum of all samples collected in a dataset, normalized by number of samples, while the root-mean-squared error is the root-mean-squared deviation from the mean spectra. Note that the VS has a slightly smaller root-mean-squared error than the GS, indicating a smaller variation. The root-mean-squared deviation between the grating spectrometer spectra and either the Virtual Spectrometer result, or the calibrated PES spectra are shown in Table S2.

Dataset	**RMS dev. (GS, PES) (meV/μJ)**	**RMS dev. (GS, VS) (meV/μJ)**
D_A	5.44	0.29
D_B	7.98	0.28
D_C	30.39	1.34

TABLE S2. Root-mean-squared deviation between the grating spectrometer spectra and either the Virtual Spectrometer or the calibrated PES for datasets D_A, D_B and D_C.

SXII. REPRODUCTION OF RESULTS

All results shown in this paper may be reproduced using the software package in `https://git.xfel.eu/machineLearning/pes_to_spec/-/tree/1.1.1/` and the data at Ref.[16] and Ref.[17]. For convenience, they have been reduced and compressed in Ref.[9]. Specifically, the following notebooks contain the software used to prepare plots shown in this manuscript:

- `https://git.xfel.eu/machineLearning/pes_to_spec/-/blob/1.1.1/notebook/Resolution%20comparison.ipynb`;
- `https://git.xfel.eu/machineLearning/pes_to_spec/-/blob/1.1.1/notebook/Toy%20resolution.ipynb`; and
- `https://git.xfel.eu/machineLearning/pes_to_spec/-/blob/1.1.1/notebook/Effect%20of%20pre-smoothing.ipynb`.

A demonstration of the software can be seen in the following notebooks.

- `https://git.xfel.eu/machineLearning/pes_to_spec/-/blob/1.1.1/demo/Demo.ipynb` shows the training and inference steps using data available in Ref.[9], which is downloaded for this purpose; and

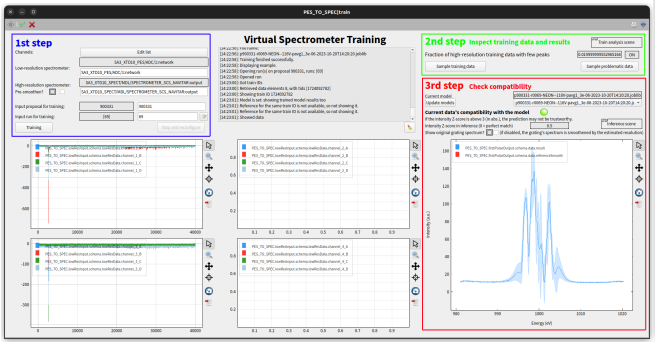

(a) Training interface.

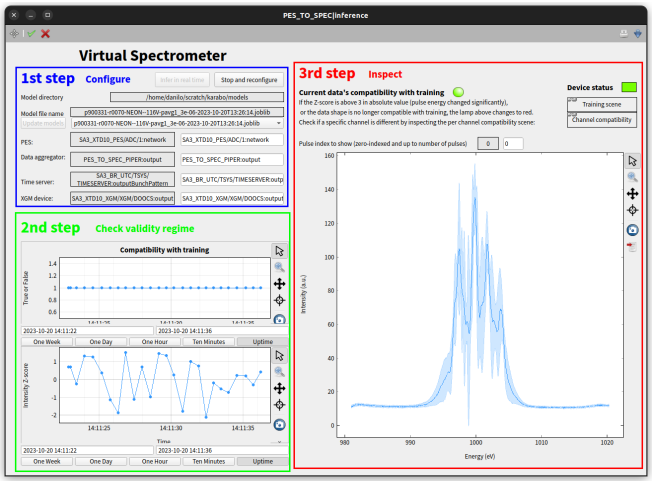

(b) VS interface to be used while the experiment progresses.

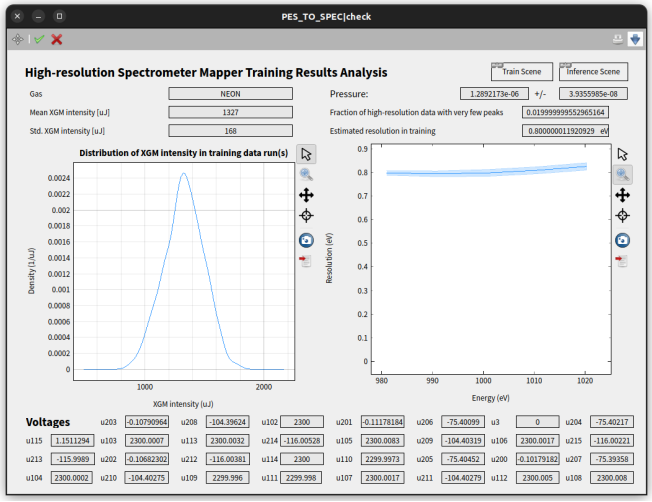

(c) Training quality checks including resolution estimate.

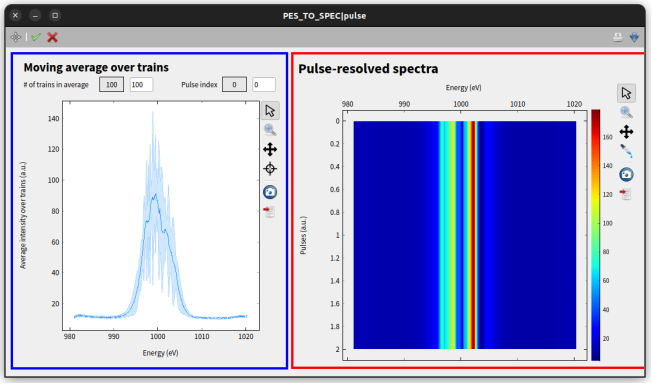

(d) Pulse-resolved inference results.

FIG. S8. Karabo graphical user interface. (a) Interface used to train the model from previously saved PES, XGM, and GS data. (b) interface to the VS, which provides the spectra in quasi-real-time using only the parasitic PES and XGM information. (c) interface available after the fit is performed, which allows the users to inspect the training quality, including the resolution achievable with the VS, relative to the GS. (d) Pulse-resolved information during inference and a moving-average representation of the pulse data over a time window.

- `https://git.xfel.eu/machineLearning/pes_to_spec/-/blob/1.1.1/demo/Demo%20only%20inference.ipynb` uses a pre-trained model in `https://git.xfel.eu/machineLearning/pes_to_spec/-/blob/1.1.1/demo/model_demo.joblib` to perform only inference using the small example dataset in `https://git.xfel.eu/machineLearning/pes_to_spec/-/blob/1.1.1/demo/demo_dataset_A_test.tar.bz2`.

REFERENCES

[1] N. Gerasimova, D. La Civita, L. Samoylova, M. Vannoni, R. Villanueva, D. Hickin, R. Carley, R. Gort, B. E. Van Kuiken, P. Miedema, L. Le Guyarder, L. Mercadier, G. Mercurio, J. Schlappa, M. Teichman, A. Yaroslavtsev, H. Sinn, and A. Scherz, Journal of Synchrotron Radiation **29**, 1299 (2022).
[2] A. Koch, J. Risch, W. Freund, T. Maltezopoulos, M. Planas, and J. Grünert, Journal of Synchrotron Radiation **26**, 1489 (2019).
[3] A. Koch, J. Risch, W. Freund, T. Maltezopoulos, M. Planas, and J. Grünert, Journal of Synchrotron Radiation **26**, 1489 (2019).
[4] M. Cardona and L. Ley, *Photoemission in Solids I*, Vol. 26 (Springer Berlin, Heidelberg, 1978).

[5]J. Laksman, F. Dietrich, J. Liu, T. Maltezopoulos, M. Planas, W. Freund, R. Gautam, N. Kujala, S. Francoual, and J. Grünert, Review of Scientific Instruments **93**, 115111 (2022).
[6]E. Saloman, J. Hubbell, and J. Scofield, Atomic Data and Nuclear Data Tables **38**, 1 (1988).
[7]C. Nicolas and C. Miron, Journal of Electron Spectroscopy and Related Phenomena **185**, 267 (2012), special Issue in honor of Prof. T. Darrah Thomas: High-Resolution Spectroscopy of Isolated Species.
[8]E. Allaria, B. Diviacco, C. Callegari, P. Finetti, B. Mahieu, J. Viefhaus, M. Zangrando, G. De Ninno, G. Lambert, E. Ferrari, J. Buck, M. Ilchen, B. Vodungbo, N. Mahne, C. Svetina, C. Spezzani, S. Di Mitri, G. Penco, M. Trovó, W. M. Fawley, P. R. Rebernik, D. Gauthier, C. Grazioli, M. Coreno, B. Ressel, A. Kivimäki, T. Mazza, L. Glaser, F. Scholz, J. Seltmann, P. Geßler, J. Grünert, A. De Fanis, M. Meyer, A. Knie, S. P. Moeller, L. Raimondi, F. Capotondi, E. Pedersoli, O. Plekan, M. B. Danailov, A. Demidovich, I. Nikolov, A. Abrami, J. Gautier, J. Lüning, P. Zeitoun, and L. Giannessi, Phys. Rev. X **4**, 041040 (2014).
[9]M. VANNONI and J. Grünert, 10.5281/zenodo.11653626 (2024).
[10]D. J. C. MacKay, in *Maximum Entropy and Bayesian Methods: Santa Barbara, California, U.S.A., 1993*, edited by G. R. Heidbreder (Springer Netherlands, Dordrecht, 1996) pp. 221–234.
[11]M. E. Tipping and C. M. Bishop, Journal of the Royal Statistical Society Series B: Statistical Methodology **61**, 611 (2002).
[12]C. Robert, *The Bayesian Choice: From Decision-Theoretic Foundations to Computational Implementation*, Springer Texts in Statistics (Springer New York, 2007).
[13]P. Welch, IEEE Transactions on Audio and Electroacoustics **15**, 70 (1967).
[14]S. W. Smith, *The Scientist and Engineer's Guide to Digital Signal Processing* (California Technical Publishing, USA, 1997).
[15]S. Hauf, B. Heisen, S. Aplin, M. Beg, M. Bergemann, V. Bondar, D. Boukhelef, C. Danilevsky, W. Ehsan, S. Essenov, R. Fabbri, G. Flucke, D. Fulla Marsa, D. Göries, G. Giovanetti, D. Hickin, T. Jarosiewicz, E. Kamil, D. Khakhulin, A. Klimovskaia, T. Kluyver, Y. Kirienko, M. Kuhn, L. Maia, D. Mamchyk, V. Mariani, L. Mekinda, T. Michelat, A. Münnich, A. Padee, A. Parenti, H. Santos, A. Silenzi, M. Teichmann, K. Weger, J. Wiggins, K. Wrona, C. Xu, C. Youngman, J. Zhu, H. Fangohr, and S. Brockhauser, Journal of Synchrotron Radiation **26**, 1448 (2019).
[16]L. Samoylova and J. Gruenert, SASE3 Photon Beam Measurements, proposal 900331 (2023).
[17]L. Samoylova and J. Gruenert, SASE3 Photon Beam Measurements, proposal 900383 (2023).

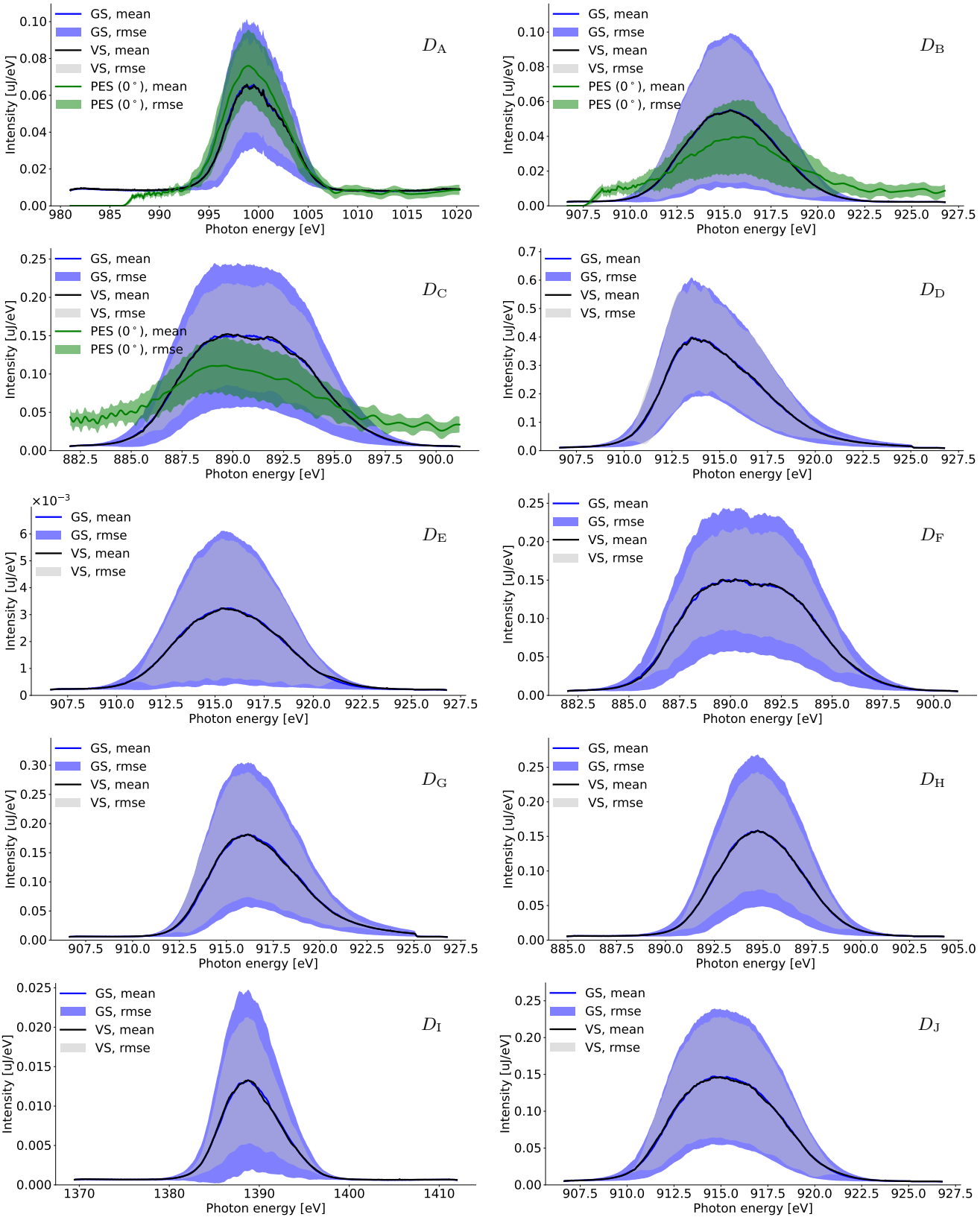

FIG. S9. Mean spectra and their root-mean-squared error of test dataset D_A – D_J measured by the grating-based spectrometer (blue) and estimated through the virtual spectrometer (black). When available, the calibrated output of the photo-electron spectrometer (green) is also shown.